Characterizing Infrasound Station Frequency Response Using Large Earthquakes and Colocated Seismometers

David Fee*[1], Kenneth Macpherson[1], and Thomas Gabrielson[2]

ABSTRACT

Earthquakes generate infrasound in multiple ways. Acoustic coupling at the surface from vertical seismic velocity, termed local infrasound, is often recorded by infrasound sensors but has seen relatively little study. Over 140 infrasound stations have recently been deployed in Alaska. Most of these stations have single sensors, rather than arrays, and were originally installed as part of the EarthScope Transportable Array. The single sensor nature, paucity of ground-truth signals, and remoteness makes evaluating their data quality and utility challenging. In addition, despite notable recent advances, infrasound calibration and frequency response evaluation remains challenging, particularly for large networks and retrospective analysis of sensors already installed. Here, we examine local seismoacoustic coupling on colocated seismic and infrasound stations in Alaska. Numerous large earthquakes across the region in recent years generated considerable vertical seismic velocity and local infrasound that were recorded on colocated sensors. We build on previous work and evaluate the full infrasound station frequency response using seismoacoustic coupled waves. By employing targeted signal processing techniques, we show that a single seismometer may be sufficient for characterizing the response of an entire nearby infrasound array. We find that good low frequency (<1 Hz) infrasound station response estimates can be derived from large ($M_w > 7$) earthquakes out to at least 1500 km. High infrasound noise levels at some stations and seismic-wave energy focused at low frequencies limit our response estimates. The response of multiple stations in Alaska is found to differ considerably from their metadata and are related to improper installation and erroneous metadata. Our method provides a robust way to remotely examine infrasound station frequency response and examine seismoacoustic coupling, which is being increasingly used in airborne infrasound observations, earthquake magnitude estimation, and other applications.

KEY POINTS

- Field-based infrasound calibration remains challenging despite recent advances.
- We use seismoacoustic coupling to characterize infrasound responses in Alaska and identify multiple issues.
- This method can characterize entire regional networks and remote arrays using colocated stations.

INTRODUCTION

Earthquakes generate infrasound through a variety of seismoacoustic coupling mechanisms. Arrowsmith *et al.* (2010) provide a review of the seismoacoustic wavefield and divide earthquake-generated infrasound into three types based on the source region: (1) “epicentral infrasound” generated by ground motion near the epicenter; (2) “secondary infrasound” from seismic surface waves shaking topography, basins, and so forth away from the epicenter; and (3) “local infrasound” from surface-wave ground motion near the infrasound receiver itself. Numerous observations of each of these phenomena have been documented (e.g., Donn and Posmentier, 1964; Kim *et al.*, 2004; Le Pichon *et al.*, 2005; Green *et al.*, 2009; Shani-Kadmiel *et al.*, 2018), and these different coupled wave mechanisms are often distinguished based on travel-time

---

1. Wilson Alaska Technical Center and Alaska Volcano Observatory, Geophysical Institute, University of Alaska Fairbanks, Fairbanks, Alaska, U.S.A., https://orcid.org/0000-0002-0936-9977 (DF); https://orcid.org/0000-0002-5521-6912 (KM); 2. Pennsylvania State University, State College, Pennsylvania, U.S.A.

*Corresponding author: dfee1@alaska.edu

Cite this article as Fee, D., K. Macpherson, and T. Gabrielson (2023). Characterizing Infrasound Station Frequency Response Using Large Earthquakes and Colocated Seismometers, *Bull. Seismol. Soc. Am.* **113**, 1581–1595, doi: 10.1785/0120220226

differences between the seismic and acoustic arrival times. Subsurface nuclear and chemical explosions have also produced seismoacoustic coupled waves, and the analysis of these waves has been shown to help determine the depth of the explosion source (Assink *et al.*, 2016; Averbuch *et al.*, 2020), which is often challenging for shallow sources using seismology alone. Of particular relevance to our study is the work of Kim *et al.* (2004), who introduced a method to verify infrasound array calibrations in the Republic of Korea using local infrasound from regional earthquakes.

In recent years, steady progress has been made on infrasound sensor calibration and quality control, but numerous challenges remain due to few ground-truth events, complicated propagation through the atmosphere, and sensor variability. Laboratory calibrations of infrasound sensors have advanced and can produce estimates of the frequency response (magnitude and phase) within 5% of a traceable standard (Merchant *et al.*, 2017; Nief *et al.*, 2018). However, these calibrations may vary over time and the sensors may be susceptible to changes in environmental conditions. In addition, multiple sensor types exist with different sensing mechanisms and electronics. Finally, wind noise reduction systems attached to the sensor often affect the frequency response, especially for the case of pipe array filters (Marty *et al.*, 2016).

Field-based infrasound calibration and frequency response estimation are particularly challenging. Relatively few ground-truth explosive events are available to use (e.g., Fee *et al.*, 2013) due to their expense and logistical complexity. Further, even with a known source the spatiotemporal variability of the atmosphere makes it difficult to use a known source to characterize an infrasound system at tens to hundreds of kilometers. Gabrielson (2011) developed a technique to use a well-calibrated reference infrasound sensor and ambient noise to characterize a colocated infrasound station response and identify problems at the station. This technique has gained widespread use. For example, numerous Comprehensive Nuclear-Test-Ban Treaty Organization (CTBTO) International Monitoring System (IMS) infrasound arrays have a separate reference sensor deployed next to each element that is used to monitor the element frequency response. This method can be effective but relies on a separate, typically expensive sensor deployed next to the primary sensor. Further, the technique relies on the reference sensor response to be stable, suitable ambient noise, and relatively low noise levels. Green *et al.* (2021) note some of the challenges of this technique, particularly identifying suitable time periods for response estimation. We note the CTBTO IMS onsite calibration requirements for each installed array is that the 0.02–4.0 Hz frequency response for the entire element (digitizer, sensor, and wind noise reduction system) should be estimated yearly, and that the magnitude should be within 5% of the laboratory calibration value. No IMS phase specification exists (Marty, 2018).

Recent expansion of the seismic and acoustic networks in Alaska, along with abundant seismicity in the region, provides a unique opportunity to study seismoacoustic coupling and evaluate station frequency response and performance. Figure 1 shows a map of the 142 infrasound stations in Alaska as of July 2020, consisting of numerous different sensor types and deployment techniques. In addition to a long-standing IMS array in Fairbanks (I53) and multiple arrays and single stations operated by the Alaska Volcano Observatory (AVO) (Power *et al.*, 2020), the EarthScope USArray Transportable Array (TA) deployed 196 infrasound sensors in Alaska and Western Canada primarily between 2014 and 2017 (Busby and Aderhold, 2020). These sensors were deployed alongside seismometers without infrasound station performance in mind, often leading to high noise levels (Macpherson *et al.*, 2022). In addition, data quality monitoring and metadata validation were not prioritized for these stations. After the TA deployment ended, the vast majority of the stations in Alaska (107 out of 158) were adopted, most of them by the Alaska Earthquake Center (AEC) and AVO and integrated into their permanent networks “AK” and “AV,” respectively.

Three energetic earthquakes with magnitudes above 7.6 occurred in Alaska between July 2020 and July 2021 (Fig. 1). These events caused widespread shaking that generated considerable local infrasound recorded by stations in the region. Here, we build off the methods introduced by Kim *et al.* (2004) and Gabrielson (2011) and use local infrasound observations to characterize station performance and derive broadband frequency response estimates of the infrasound stations across Alaska. First, we evaluate the method using a single element from the well-understood I53 infrasound array and nearby COLA seismic station. We then expand this analysis between all eight I53 elements and COLA. We find that good low frequency (<1 Hz) infrasound station response estimates can be derived out to at least 1500 km. The response of multiple stations in the region is found to differ considerably from their metadata and are likely related to improper installation and inaccurate metadata. We also find a single seismometer may be sufficient for characterizing the response of an entire infrasound array assuming sufficiently low noise levels. The data set and techniques used here may be broadly applicable to other regions and scientific problems in geophysics. We note that K. A. Macpherson *et al.* (unpublished manuscript, see Data and Resources) use a complementary application of local infrasound to derive seismic velocity and earthquake magnitudes.

DATA

We use data from stations with colocated seismoacoustic sensors across Alaska between July 2020 and July 2021 (Fig. 1). During this period, 142 infrasound stations were present in Alaska, with arrays and single sensors each counted as a single station. This includes 102 Alaska Regional Seismic network (AK) stations, 38 AVO stations, one IMS array, one Global

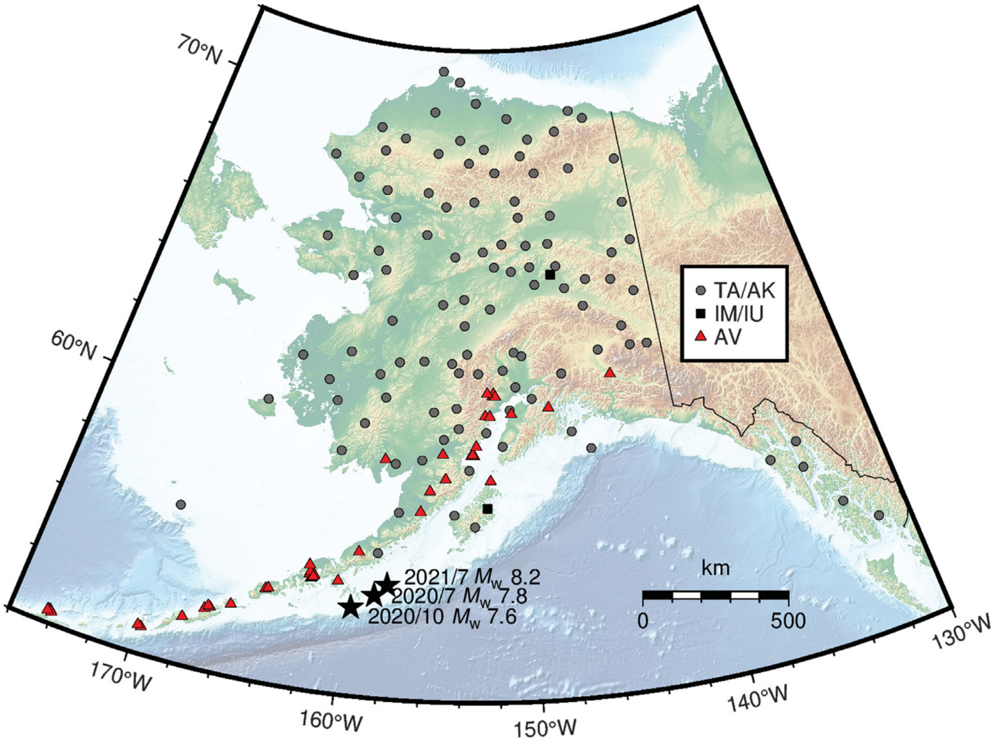

Figure 1. Map of infrasound stations in Alaska in 2020–2021. Each station's marker indicates the network: circles indicate TA/AK, squares indicate IM/IU, and triangles indicate AV. All but one station has a colocated seismometer. The locations of the three large earthquakes used in this study are plotted as stars.

Seismograph Network (GSN)—Incorporated Research Institutions for Seismology (IRIS)/International Deployment of Accelerometers (IDA) (II) station (KDAK), and one GSN—IRIS/U.S. Geological Survey (USGS) (IU) station (COLA). Of these stations, 141 have seismometers deployed within 2 km, and we choose these stations to analyze here. For infrasound arrays, we only select the infrasound element closest to the seismometer unless noted. We select the I53 IMS infrasound array and COLA IU seismic station in Fairbanks, Alaska, for detailed analysis as these stations recorded all three earthquakes with good signal-to-noise ratios (SNRs) and both stations have a well-understood, validated response. We process the broadband seismic component nearest the surface where a borehole is also available.

We use temperature and absolute pressure estimates when available to compute local sound speed and air density. However, only a small fraction of the stations in Alaska have associated meteorological data. Therefore, in cases where we do not have local temperature and air density data we use nominal values of 15°C and 1013 hPa, respectively. For I53, absolute pressure is recorded at the H6 element and temperature at H7.

We select three large earthquakes that occurred along the Alaska–Aleutian subduction zone between July 2020 and 2021 for analysis (Fig. 1). An M_w 7.8 earthquake occurred on 22 July 2020 at 28 km depth. A few months later, on 19 October 2020, an M_w 7.6 earthquake occurred nearby at 31 km depth. On 29 July 2021, yet another significant earthquake occurred nearby. This time an M_w 8.2 occurred south of Perryville, Alaska, on 29 July 2021 at a depth of 35 km. These three earthquakes had epicenters within approximately 140 km of each other, produced notable ground motion detected across the region and world, and as we discuss later, considerable local infrasound detected across Alaska. Although interesting, we do not consider the different earthquake source mechanisms or features in our analysis as we are primarily concerned with local ground motion at the colocated seismoacoustic stations. We refer the reader to recent papers such as Elliott *et al.* (2022) and Xiao *et al.* (2021) for more information on these earthquakes.

METHODS

We combine the methods of Kim *et al.* (2004) and Gabrielson (2011) to analyze the frequency response of the infrasound station. Low-frequency pressure changes at the Earth's surface from ground motion, here termed p_1, can be estimated using a simple relationship:

$$p_1 = \rho c v, \tag{1}$$

in which ρ is the air density, c is the local sound speed, and v is the vertical ground velocity (Donn and Posmentier, 1964). The product of the air density and sound speed is termed the specific acoustic impedance and assumes the wave generation is planar. From equation (1), the local pressure changes (infrasound) from ground motion can be computed if a colocated seismometer records vertical ground velocity and reasonable estimates of air density and sound speed are known. Using standard values of $c = 340$ m/s and $\rho = 1.2$ kg/m^3, $p_1/v = 408$ Pa/m/s. This value provides a quick way to check colocated seismoacoustic waveforms to determine whether local infrasound is being produced by ground motion.

Kim *et al.* (2004) used colocated seismoacoustic stations to verify infrasound sensor calibrations at two arrays in the

Republic of Korea. They computed the transfer function, or gain $\hat{g}$, between the infrasound and vertical seismic velocity in the frequency domain:

$$\hat{g} = \frac{S_I}{S_S}, \tag{2}$$

in which S_I is the infrasound spectra with units of Pa/Hz and S_S is the seismic spectra with units of m/s/Hz. They then compared the transfer function with the acoustic impedance ($\rho \times c$). They found that the infrasound calibrations generally agree between 0.03 and 0.1 Hz, but there was considerable scatter (tens of dB) at higher frequencies. This novel application provides useful information on the magnitude (amplitude) of the frequency response, but it does not provide any information on the phase or level of confidence in the estimates. Division of the spectra often produce considerable scatter (Gabrielson, 2011). Watada *et al.* (2006) also verified local infrasound coupling by comparing both the amplitude and phase of the coupled waves with a theoretical model.

Gabrielson (2011) introduced a method for characterizing infrasound station frequency response by utilizing a well-calibrated, stable reference sensor next to the element:

$$H_I = H_R \frac{\overline{G_{II}}}{\overline{G_{IR}}}, \tag{3}$$

in which H_R is the complex reference sensor response, $\overline{G_{II}}$ is the averaged autospectral density of the infrasound sensor data, and $\overline{G_{IR}}$ is the averaged cross-spectral density between the reference sensor and infrasound element. Using the cross-spectral density and spectral averaging reduces incoherent noise between the infrasound and reference sensor and overall scatter in the spectral estimates. This method has now been widely adopted in the IMS and is helping to address difficulties of in situ calibration of infrasound stations. We note either the spectral density or power spectrum is valid in equation (3).

Using equations (1)–(3), we can derive the infrasound response from the seismometer and acoustic impedance. Treating the seismometer as the "reference" sensor and combining equation (1) with equation (3), we can derive the complex infrasound frequency response, H_I, from local infrasound-based vertical velocity:

$$H_I = H_S \frac{\overline{G_{II}}}{\rho c \overline{G_{IS}}}. \tag{4}$$

The relative infrasound magnitude and phase can then be retrieved from $\frac{H_I}{H_S}$. Gabrielson (2011) discuss two forms of relative sensor characterization, depending on whether the incoherent (noise) component of the data being compared is likely in the reference sensor (S) or infrasound element (I). For infrasound element to reference sensor comparisons, the incoherent component is often in the reference sensor data because it lacks noise reduction, and equation (4) is preferable. Because the actual local infrasound source here is assumed to be the vertical ground velocity, we suggest the incoherent portion is more likely to be in the infrasound data and use a modified form of relative characterization from Gabrielson (2011):

$$H_I = H_S \frac{\overline{G_{IS}^*}}{\rho c \overline{G_{SS}}}, \tag{5}$$

in which $*$ indicates the complex conjugate. Comparing derived frequency responses between the two methods suggests this is a valid assumption for our scenario. In this article, we compute the relative response of the infrasound compared to the seismic velocity:

$$\frac{H_I}{H_S} = \frac{\overline{G_{IS}^*}}{\rho c \overline{G_{SS}}}. \tag{6}$$

In addition, we remove the response from the seismic and acoustic data prior to deriving the infrasound frequency response from equation (6) using the available metadata and frequency-based deconvolution in ObsPy (Beyreuther *et al.*, 2010). In the deconvolution, we use a cosine-tapered band-pass filter between 10,000 s and the Nyquist frequency to reduce overamplification of very low frequencies. Therefore, the magnitude and phase we report, $\frac{H_I}{H_S}$, represents the deviation from the expected infrasound response (i.e., a 0 dB offset in magnitude corresponds to the expected magnitude response and a 6 dB offset in magnitude represents a factor of 2 deviation).

The local sound speed c and air density ρ for dry air can be approximated from the temperature and absolute pressure utilizing the ideal gas law:

$$c = \sqrt{\gamma R T}, \tag{7}$$

$$\rho = \frac{P}{R_s(T + 273.15)}, \tag{8}$$

in which $R_s = 287\ \mathrm{J/(kg \cdot K)}$ is the universal gas constant, T is the temperature in Celsius, and P is the absolute pressure in pascals (Pierce, 2019).

The magnitude-squared coherence, simply referred to as coherence hereafter, between the infrasound and seismic data can be used as a measure of confidence in the response estimate (Gabrielson, 2011). For our scenario the coherence is estimated using:

$$\gamma_{IS}^2 = \frac{|\overline{G_{IS}}|^2}{\overline{G_{II}}\,\overline{G_{SS}}}. \tag{9}$$

High coherence values indicate strong similarity between the infrasound data and seismic velocity. We note that our method assumes the seismometer response H_S is well characterized and stable, the vertical velocity is linear, and estimates of the sound speed and air density are available and/or reasonable.

We note that the vertical displacement of the infrasound sensor, via ground motion or otherwise, will also produce detectable pressure changes, which we term p_2:

$$p_2 = \rho g \Delta z, \tag{10}$$

in which g is the acceleration of gravity and Δz is the vertical displacement of the sensor. p_1 is proportional to velocity whereas p_2 is proportional to displacement. If the amplitude of Δz is held constant, as frequency increases, velocity would increase; therefore, the ratio of p_1 to p_2 would also increase. Above some frequency, p_1 will dominate.

To determine at what frequencies p_1 will dominate for local infrasound production over p_2 resulting from displacement of the sensor, we set p_1 equal to p_2, assume sinusoidal motion in which $v = 2\pi f \Delta z$, and solve for f:

$$p_1 = p_2, \tag{11}$$

$$\rho c 2\pi f \Delta z = \rho g \Delta z, \tag{12}$$

$$f = \frac{g}{2\pi c}. \tag{13}$$

For $g = 9.8\ \mathrm{m/s^2}$ and the values noted above for c and ρ, p_1 should be dominant above $f = 0.0046$ Hz. We, therefore, use caution in interpreting frequency response estimates below this frequency and restrict most of our analysis to frequencies above 0.05 Hz (about 10 times the crossover frequency). We also note that there should be a 90° phase difference between the vertical velocity and acoustic data for p_2 whereas for p_1 they should be in phase.

The infrasound sensor may also be sensitive to ground-motion acceleration, sometimes referred to as mechanical, seismic, or acceleration sensitivity. We assume sinusoidal motion and define the acceleration sensitivity as

$$p_3 = \alpha 2\pi f v, \tag{14}$$

in which α is the apparent pressure per input acceleration. This value is highly dependent on the sensor type and mechanics. To solve for the crossover frequency, above which the acceleration response will dominate, we set p_1 equal to p_3 and solve for f:

$$f = \frac{\rho c}{2\pi \alpha}. \tag{15}$$

For the sensors used in this study α is estimated to be between 0.04 and 0.10 $\mathrm{Pa/m/s^2}$ (Merchant *et al.*, 2017; Nief *et al.*, 2018). The crossover frequency in which p_3 dominates would then be roughly 1620–650 Hz, which is well above frequencies we analyze. We note that other infrasound sensor types have higher acceleration sensitivity that may interfere in the infrasound band (Merchant and McDowell, 2014).

Acoustic-seismic coupling is also common (e.g., Bishop *et al.*, 2022) and may have similar waveform characteristics to seismoacoustic coupling, but again should have a 90° phase difference (Ichihara *et al.*, 2012) and amplitude ratios should be inconsistent with local infrasound generation described earlier.

We process colocated seismoacoustic data across Alaska for 15 min data segments for the three large regional earthquakes described earlier. The analysis window start time is derived by calculating *P*-wave arrival times from the hypocenter to the seismic station location using the IASPEI91 velocity model (Kennett and Engdahl, 1991) and origin times from the Advanced National Seismic System Composite Catalog (U.S. Geological Survey [USGS], 2017). We compute the infrasound response from equation (6) and coherence from equation (9) between 0.02 and 8.0 Hz for these windows in 200 s segment lengths with 90% overlap between segments. This provides 36 time estimates for each station pair per earthquake. The spectral estimates are computed using a 50 s window in each segment with 50% overlap, providing a spectral resolution of 0.02 Hz. Similar to Marty *et al.* (2016) and Green *et al.* (2021), we apply "subwindow" processing where we only select time–frequency segments that exceed a threshold coherence for our response estimates. We choose a coherence threshold of 0.7. Subwindow processing ensures only highly similar time and frequency portions of the data are used in the spectral estimate, at the expense of fewer spectral estimates and potentially higher variance. We require a minimum of 10 subwindows at each frequency to save the spectral estimate. The subwindow processing is useful for our scenario as we typically have band-limited signals and occasionally poor SNR. Spectral estimates are performed using the Welch periodogram method. The CTBTO IMS band of interest for infrasound stations is 0.02–4.0 Hz and nominal calibration frequency is 0.25 Hz, so we focus our analysis on those regions but discuss higher frequency response estimation, too. We report our magnitude values in both dB and percent from nominal, and the phase in degrees from 0. We note the IMS infrasound calibration specification of 5% corresponds to 0.42 dB.

Relative seismic travel time between the seismometer and infrasound station is calculated by assuming a 3.5 km/s seismic surface-wave velocity because this is the most prominent seismic wave observed for these events. We subtract this travel time from the infrasound sensor to effectively place it at the seismometer. For most colocated stations this travel time is negligible, but it does become more important for the full array analysis. In the case where the sample rates differ between the seismic and infrasound data, we resample both to the lower of the two sample rates using Lanczos interpolation in ObsPy.

We also compute probabilistic power spectral densities (PPSDs) for some stations to investigate potential station issues identified from our seismoacoustic coupling method. Our method follows that of Macpherson *et al.* (2022), which uses the framework of McNamara and Buland (2004) and ObsPy. The infrasound PPSDs are plotted against the AK region infrasound noise models of Macpherson *et al.* (2022). We choose 30 min PPSD window lengths with 50% overlap.

RESULTS AND DISCUSSION

Seismic and infrasound data for the COLA seismic and I53 infrasound stations show remarkable similarity for all three earthquakes, and we are able to derive good frequency response estimates over a fairly broad frequency range. These stations are located in interior Alaska at over 1200 km from the earthquake hypocenters. Figure 2a,b shows the 0.02–8.0 Hz seismic (black) and infrasound (blue) data for the 22 July 2020 earthquake. Relative amplitudes, durations, and waveform features are highly similar between the seismic and infrasound data. We derive the frequency response for I53H1 using equation (6) and the method outlined earlier and plot the coherence over time and magnitude and phase for I53H1 for this earthquake in Figure 2c–e, with each frequency estimate colored by the coherence. We obtain high coherence and, therefore, good frequency response estimates between ≈0.02 and 1 Hz, and low coherence above 2 Hz. The magnitude and phase are relatively flat between 0.02 and 1 Hz: less than ±1 dB (12%) and ±15°. There is increased scatter around 0.1 and 1–2 Hz. The coherence drops off rapidly above ≈1.5 Hz and prevents reliable response estimates. At 0.25 Hz, the magnitude, phase, and coherence values for this event and station pair are −0.37 dB (−4.13%), −6.3°, and 0.96, respectively. These results provide confidence in our methods and verification of the seismic and infrasound frequency responses for these stations.

We compute the magnitude for the same event for COLA-I53H1 using the autospectral density-based transfer function in equation (2) and plot it in Figure 2d. We divide equation (2) by the acoustic impedance to get the magnitude in decibels relative to 0. Compare these results to the averaged cross-spectral density method results (equation 6) shown in the same subplot. Below 0.5 Hz, the magnitude estimates are relatively flat and hover near 0, in line with the calibration values and averaged cross-spectral density method. At higher frequencies, we see increasing scatter and by 1.0 Hz magnitude estimates show an overall shift (bias) to positive magnitudes. With this method it is impossible to tell what frequency estimates are trustworthy and which are not. The greater variance, lack of estimate quality information, bias, and missing phase information are all consistent with expectations described in the Introduction. Figure 2d has similar trends as the transfer functions shown in Kim *et al.* (2004).

Figure 3 shows a plot of the waveforms, coherence over time, and frequency response for the 19 October 2020 M_w 7.6 event for COLA and I53H1. Similar to Figure 2, we note very high coherence and good response estimates between 0.02 and 0.2 Hz followed by slightly lower coherence and greater scatter in the response estimates between 0.2 and 1.5 Hz. Above 1.5 Hz, low coherence limits reliable response estimates. Magnitude and phase estimates are very close to zero during high coherence periods and show increasing scatter and deviations for lower coherence. At 0.25 Hz, the magnitude, phase, and coherence values for this event are −0.22 dB (2.57%), −11.7°, and 0.88, respectively.

Figure 4 shows similar results at COLA–I53H1 for the 29 July 2021 M_w 8.2 event. This is the largest magnitude event of the three and had the highest amplitudes at I53 and COLA. We find high coherence and good response estimates between 0.02 and 0.5 Hz followed by slightly lower coherence and greater scatter in the response estimates between 0.5 and 1.2 Hz. Above 1.2 Hz, the low coherence again limits response estimates. Similar to the other events, magnitude and phase estimates are very close to zero during high coherence periods and show increasing scatter and deviations for lower coherence. At 0.25 Hz, the magnitude, phase, and coherence values for this event are −0.56 dB (−6.66%), −7.2°, and 0.92.

Seismoacoustic coherence at COLA–I53H1, and subsequent frequency response estimates, mirror the seismic wave energy arrivals for all three earthquakes (see Figs. 2–4c). The *P* wave arrives first with broadband energy from approximately 0.1–5 Hz and is short duration, followed by another short duration *S*-wave arrival with lower frequency energy. The surface waves dominate below 1 Hz and have the highest amplitudes, coherence, and longest duration. The infrasound frequency response estimate is a combination of energy from all of these wave types, although each contributes different amounts. We note that in our scenario the *P* wave is solely response for high-frequency seismoacoustic coupling, and its lower amplitude and short-duration limits our ability to estimate the frequency response and performance above 1 Hz.

We find that seismic-acoustic coupling between COLA and I53 is sufficient to derive the frequency response for all eight infrasound array elements, despite the fact that the array is distributed over an approximately 2 × 2 km area. Figure 5 shows the I53 array geometry and COLA seismic station. The gray arrow indicates the direction of arrival of seismic waves from the 2020 July earthquake. Table 1 lists the 0.1 and 0.25 Hz magnitude, phase, and coherence values for all eight I53 elements from this event derived using seismoacoustic coupling. We find similar coherence and response estimates for all elements. Coherence is very high (>0.92) at 0.1 Hz, and still very good (>0.88 Hz) at 0.25 Hz. Magnitude and phase values at 0.1 Hz range from −0.51 to 0.88 dB (−5.66% to 10.64%)

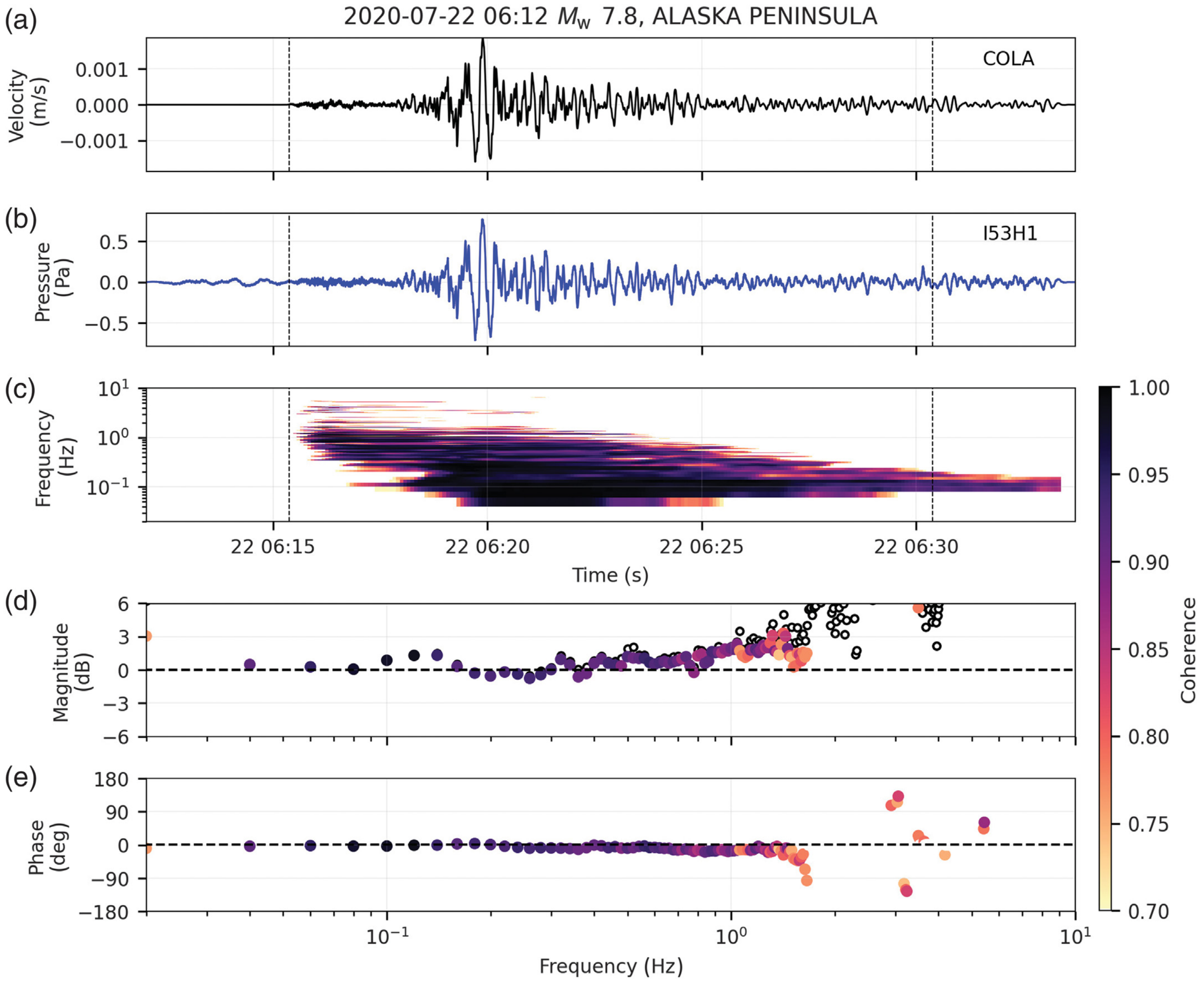

Figure 2. Waveforms, coherence, and frequency response (magnitude and phase) for the 22 July 2020 M_w 7.8 earthquake at I53H1 and COLA. (a,b) The 0.02–8.0 Hz seismic and infrasound data, respectively. (c) Coherence over time between 0.02 and 10 Hz. The two dashed vertical lines indicate the time period analyzed. (d,e) Magnitude and phase. Each frequency response estimate is colored by the coherence. The white circles with black outline indicate the magnitude estimated from the autospectral density-based transfer function from equation (2). High waveform similarity and coherence is present between the two waveforms, particularly at frequency below 1.0 Hz. Magnitude and phase estimates are both roughly flat and near zero up until ≈1.0 Hz. Poor coherence limits estimates above 1.5 Hz.

and −4.83° to −0.86°. At 0.25 Hz, the magnitude and phase range from −1.48 to 0.56 dB (−15.64% to 6.65%) and −6.32° to 8.63°, respectively. Most of these values are within 5% of the calibration value, suggesting that (1) the calibrations are accurate and (2) our seismoacoustic coupling method is sufficient to examine the frequency response of an entire infrasound array with a single seismometer. We acknowledge some natural variability and uncertainty in the existing metadata and calibrations. Phase values may deviate slightly due to an assumed single seismic-wave speed. In addition, there is no obvious trend between the coherence or response estimates and array location or distance from the seismometer to infrasound sensor. Straight-line distances between COLA and the eight I53 elements range from 0.15 to 1.7 km. The much longer wavelength of the seismic wave (∼14 km at 0.25 Hz for a 3.5 km/s surface wave) compared to the size of the infrasound array likely contributes to the excellent coherence across the array. There is also relatively low (≈58 m) maximum elevation difference between the sites, whereas other arrays may have greater elevation differences that could lead to increased uncertainty.

Next, we apply our technique to all colocated seismoacoustic stations operating in the region during the 19 October 2020 earthquake. We choose this earthquake because it had the greatest low-frequency coherence and decent overall SNR at

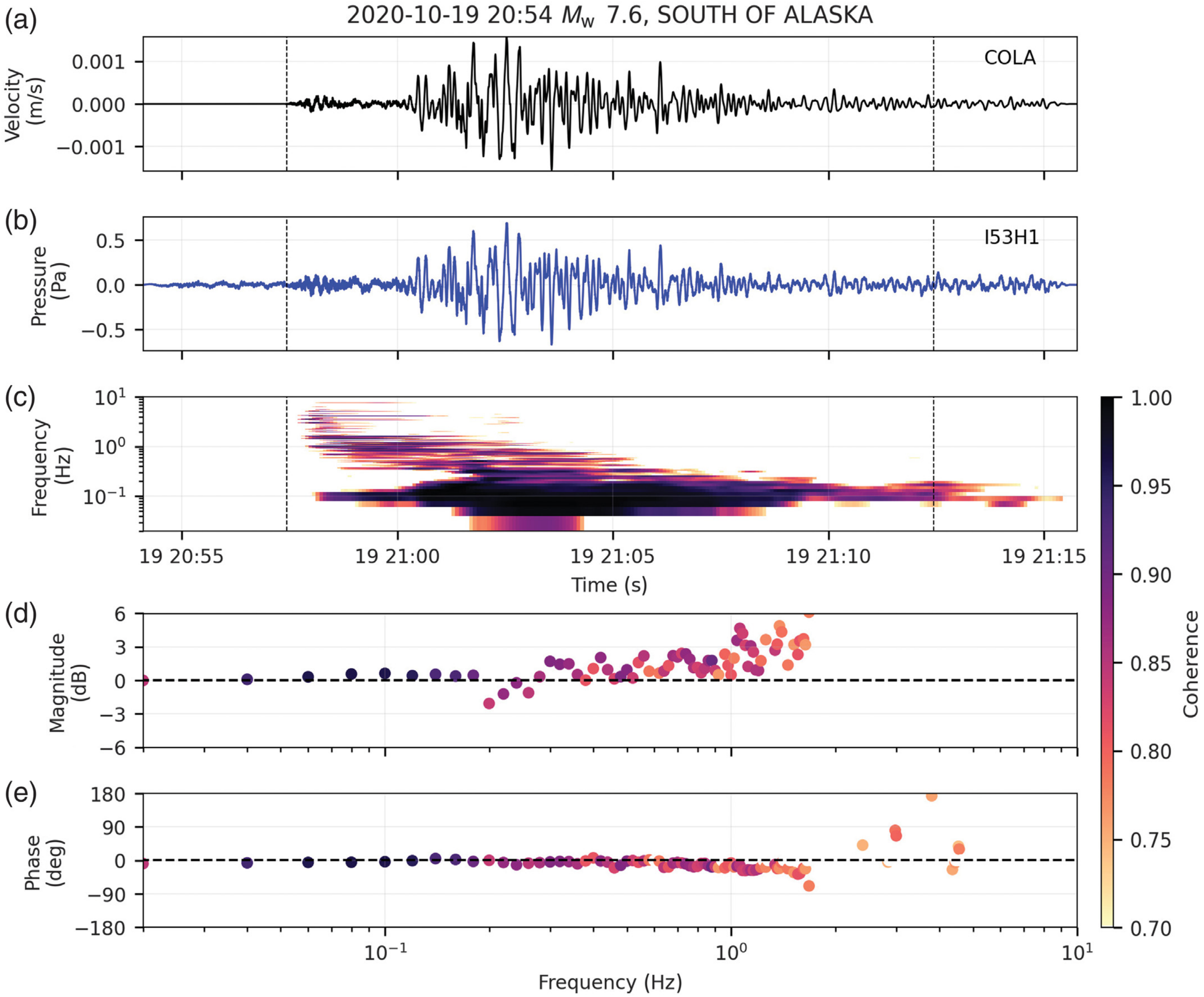

Figure 3. Waveforms, coherence, and frequency response for the 19 October 2020 M_w 7.6 earthquake at I53H1 and COLA. (a,b) Seismic and infrasound data, (c) coherence, (d) magnitude, and (e) phase. Figure layout is the same as in Figure 2. High waveform similarity, coherence, and good frequency response estimates are present between approximately 0.02 and 0.2 Hz and to a lesser extent from 0.2 to 1.0 Hz.

many stations. Further, some of the TA stations had been removed in summer 2021 (Busby and Aderhold, 2020) prior to the M_w 8.2 in July 2021. Figure 6 shows the 0.1 (Fig. 6a) and 1.0 Hz (Fig. 6b) magnitude estimates for each station. The symbol color indicates the magnitude (red above 0, blue below 0) and the symbol size the coherence. Stations with low coherence (below 0.7) or with no data are denoted as smaller gray circles. First, many more reliable estimates (high coherence) are available at 0.1 Hz compared to 1.0 Hz, which is consistent with the I53 analysis. Of the 142 stations installed during this period, 67 have coherence >0.7 at 0.1 Hz and 19 at 1.0 Hz. We note that many stations with low coherence are located in coastal regions. This is primarily due to higher infrasonic noise levels at these stations, consistent with the findings of Macpherson *et al.* (2022). They found that the noise levels at many of these sites were very high due to their location in exposed, windy areas. Multiple stations with sufficient coherence show notable deviations from their expected frequency response at both 0.1 and 1.0 Hz. At 0.1 Hz, eight stations have magnitudes that deviate >3 dB from their calibrations. At 1.0 Hz, four stations have deviations >3 dB. We do not examine phase response for the entire network in detail here but note that most are flat unless installation issues are suspected (discussed later).

AK network station CHUM (Lake Minchumina, AK: 63.8827, −152.3152) has a very low magnitude response across all frequencies. Figure 7 shows the CHUM waveforms, coherence over time, and magnitude and phase. Seismic and infrasound waveforms generally show similar features and relative

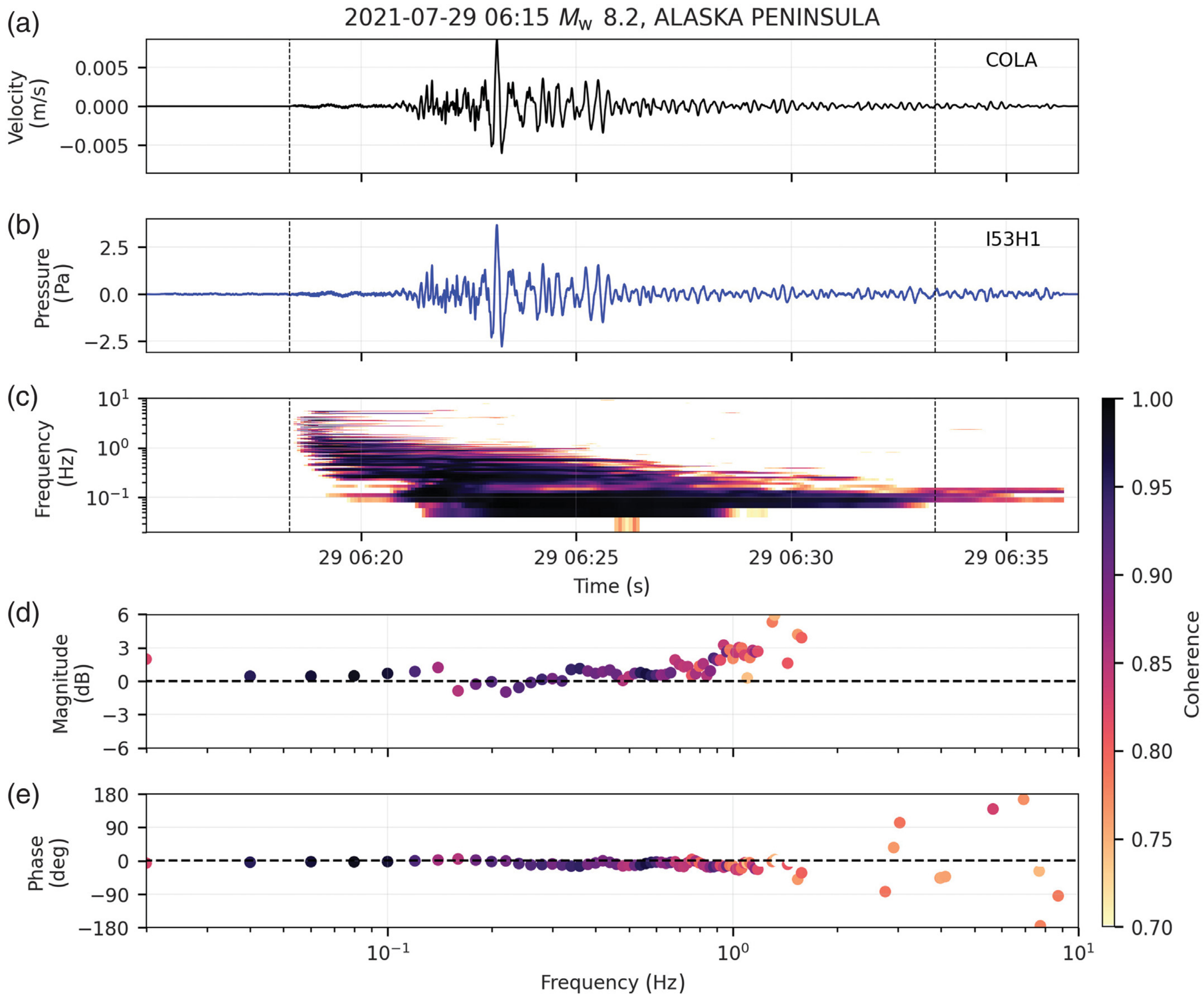

Figure 4. Waveforms, coherence, and frequency response for the 29 July 2021 M_w 8.2 earthquake at I53H1 and COLA. (a,b) Seismic and infrasound data, (c) coherence, (d) magnitude, and (e) phase. Figure layout is the same as in Figure 2. High coherence and good frequency response estimates are available between 0.02 and 0.5 Hz, followed by decreased coherence at higher frequencies.

amplitudes, and there is high coherence between 0.02 and 1 Hz. Examining the frequency response shows there is a consistent −26 dB (2000%) offset in the magnitude while the phase is flat. Comparing this response to the PPSDs for September 2020 (Fig. 8a) shows consistently low noise levels at all frequencies and below the AK infrasound noise model. As noted by Macpherson *et al.* (2022), this station is one of four AK network stations (CAPN, CHUM, CUT, and L20K) that exhibit response issues. Our analysis also shows CAPN, CUT, and L20K to have notable deviations in the magnitude (Fig. 6).

Another station with a notable deviation in the response is HARP (Gakona, AK: 62.3987, −145.1568) (Figs. 6, 9). The seismic and acoustic waveforms have similar features and relative magnitudes. There is high, broadband coherence, including decent coherence up to approximately 3 Hz. The magnitude and phase at very low frequencies (<0.1 Hz) is relatively flat and at the expected values. However, the magnitude, and to a lesser extent the phase, deviates considerably at higher frequencies. At 1 Hz, the magnitude is reduced by approximately 12 dB (400%) and the phase is offset by up to 45°. Examination of the PPSD (Fig. 8) shows that the noise levels are low but still almost all above the AK low noise model. The general shape of the PPSD also generally follows the $1/f$ rolloff expected for ambient infrasound noise (Brown *et al.*, 2014; Macpherson *et al.*, 2022). However, our seismoacoustic coupling method suggests a clear issue in the frequency response. This highlights the utility of our method and how it can be complementary to PPSD noise analysis.

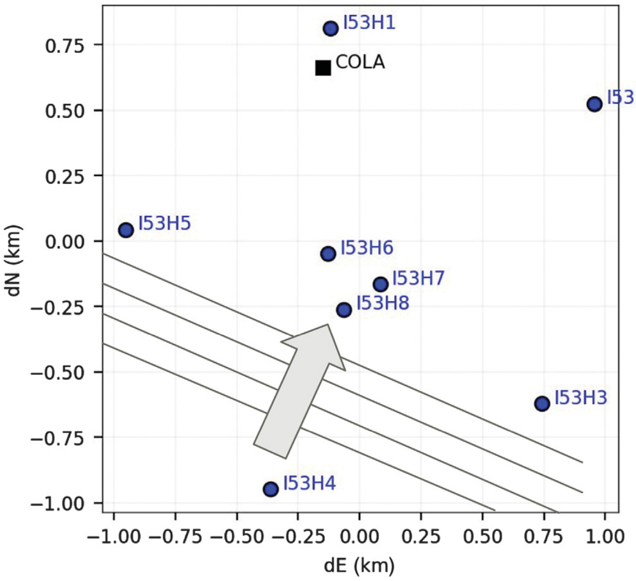

Figure 5. Map of the I53 infrasound array (blue circles) and COLA seismic station (black square). The earthquake wave arrival direction is indicated by the gray arrow.

We consulted with the engineers and personnel responsible for maintaining the AK station metadata and relayed the issues identified in this analysis and those in Macpherson *et al.* (2022). These conversations resulted in identification of incorrect metadata at the IRIS Data Management Center (DMC) for four stations (CHUM, COLD, CUT, KNK, and SSN), where the gains were off by a scaling factor between ∼4 and 24. This is consistent with our analysis and Figure 7. These metadata issues were corrected in early 2022, and reanalysis of the noise PPSDs and seismoacoustic coupling show they now have reasonable noise levels and the expected frequency response when sufficient coherence is present. We also identified installation issues at four stations (HARP, CUT, CAPN, and MLY), where the infrasound sensors were indeed not ported to the atmosphere and were only recording pressure changes inside the instrument hut. This is consistent with the notable, somewhat unpredictable response deviations identified in Figure 9 and also in applying our technique to CUT and CAPN. The seismoacoustic coherence is too low for meaningful response estimates at MLY, although it was noted by the engineers that it too was not ported to the atmosphere.

Finally, we also note that estimates of the acoustic impedance may vary substantially at a single station throughout the year, as well as across a region. These estimates will affect the frequency response estimate accuracy. For example, Figure 10 shows the sound speed, density, and acoustic impedance ($c \times \rho$) for element 7 at I53 in Fairbanks, Alaska, for the year 2020. The local temperature and atmospheric pressure are recorded at the array and the sound speed and density are computed via equations (7) and (8). We find that the sound speed varies between 305 and 348 m/s, density between 1.14 and 1.52 kg/m^3, and impedance contract between 392 and 463 Pa/m/s. Therefore, the impedance contrast for this site varies 18% throughout the year, and assuming a single impedance contrast value could add considerable uncertainty to the

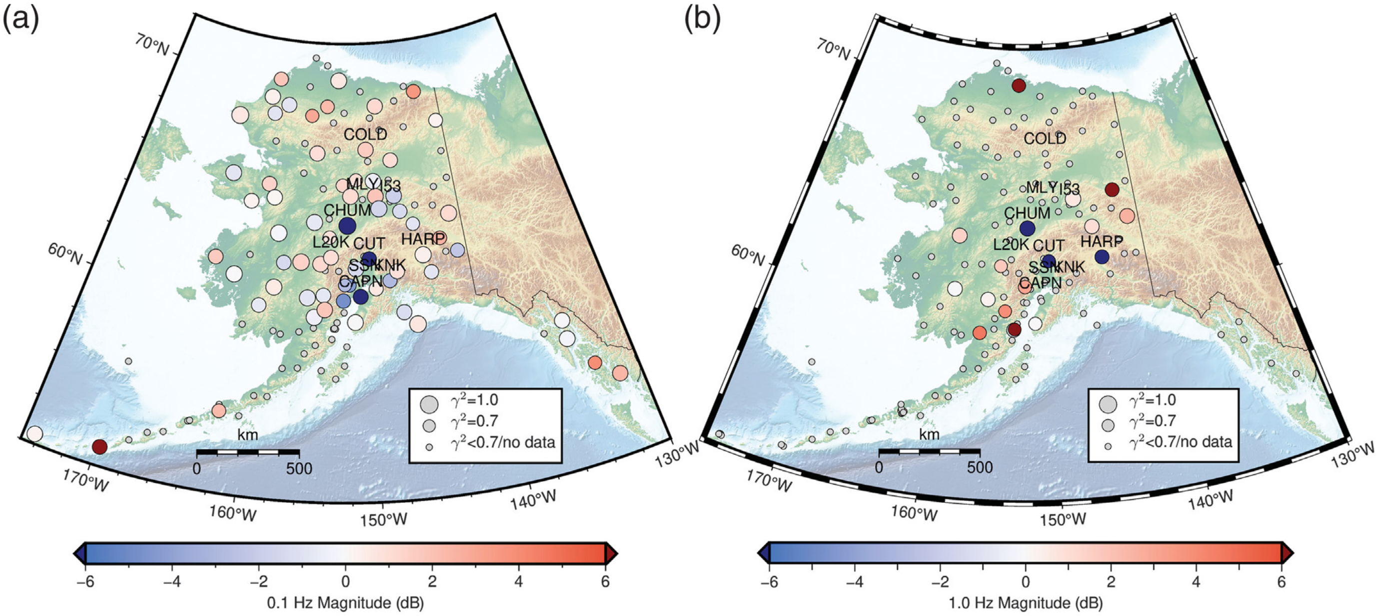

Figure 6. Magnitudes estimates at (a) 0.1 and (b) 1.0 Hz for infrasound stations in Alaska for the 2020 October earthquake. Stations are plotted as circles, with the color indicating the seismoacoustic coupling response estimate. Red values are deviations above zero and blue below zero. The size of the circle indicates the coherence value or no available data. Names of stations mentioned in the text are listed above the symbol. Multiple stations with notable deviations are identified at each frequency. Higher coherence and more response estimates are available at lower frequencies.

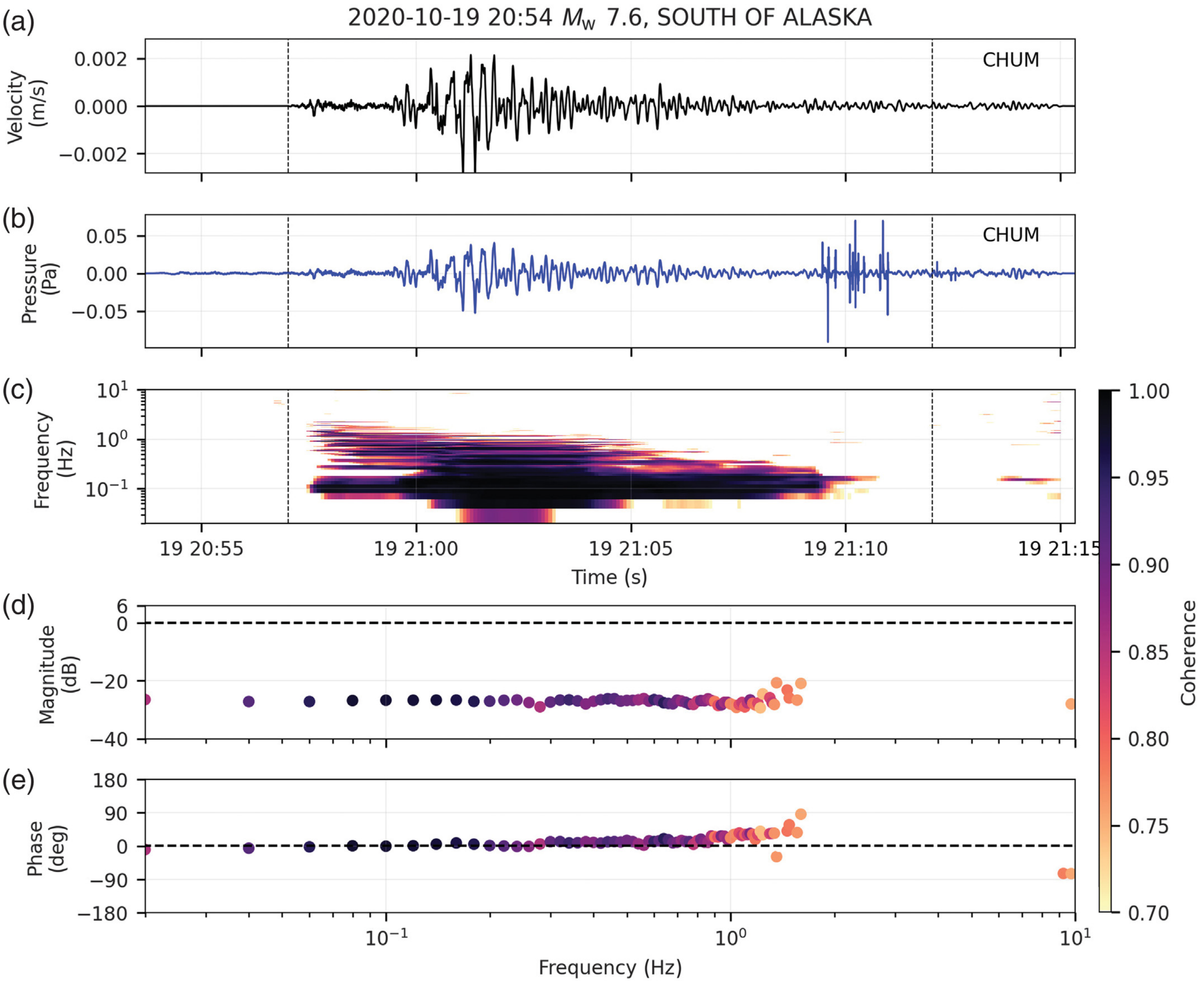

resulting coupled infrasound wave and the response estimate. The meteorological data are not available for most of the stations we use as they are in remote areas. Future work could incorporate more accurate estimates of sound speed and air

Figure 7. Waveforms, coherence, and frequency response for the 19 October 2020 M_w 7.8 earthquake at CHUM. (a,b) Seismic and infrasound data, (c) coherence, (d) magnitude, and (e) phase. Figure layout is the same as Figure 2. Note the consistent but very low magnitudes.

TABLE 1
I53—COLA Magnitude, Phase, and Coherence for the 22 July 2020 Earthquake at 0.1 and 0.25 Hz

	0.1 Hz				0.25 Hz			
Element	**Magnitude (dB)**	**Magnitude (%)**	**Phase (°)**	**Coherence**	**Magnitude (dB)**	**Magnitude (%)**	**Phase (°)**	**Coherence**
H1	0.08	0.89	−2.98	0.97	−0.37	−4.13	−6.32	0.94
H2	0.21	2.45	−0.86	0.98	−0.50	−5.58	8.05	0.92
H3	−0.51	−5.66	−1.99	0.92	−1.48	−15.64	5.94	0.88
H4	0.88	10.64	−3.98	0.96	−0.09	−1.06	5.42	0.88
H5	0.52	6.21	−3.48	0.96	0.56	6.65	3.91	0.90
H6	0.06	0.65	−4.56	0.95	0.55	6.51	5.70	0.92
H7	0.23	2.70	−4.83	0.93	0.45	5.35	7.29	0.91
H8	0.34	4.02	−3.63	0.94	0.07	0.86	8.63	0.90

Magnitudes are listed in decibels and percent from the calibration values.

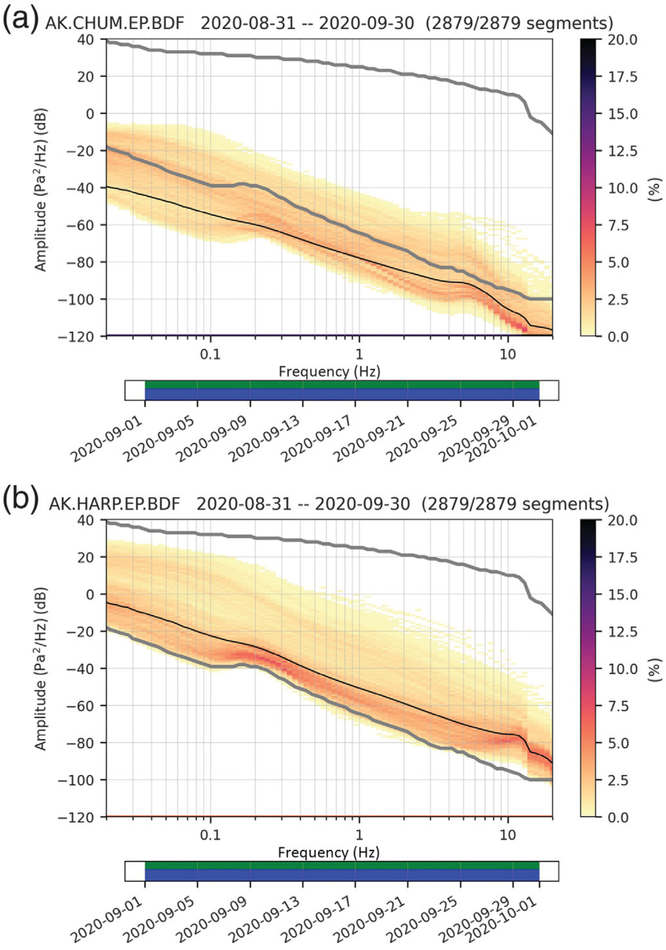

Figure 8. Probability power spectral density (PPSD) for stations (a) CHUM and (b) HARP. Data are processed between 1 September and 1 October 2020. Spectra are shown relative to the AK noise models of Macpherson *et al.* (2022) (gray lines). The mean spectra are plotted as a black line. The bottom of each subplot indicates data segments available (blue bars) and data segments used in the computation (green bars).

density using atmospheric model or reanalysis data, or by adding meteorological equipment to the stations.

CONCLUSIONS

We use seismoacoustic coupling from three recent large earthquakes in Alaska to examine infrasound station frequency response. Our method builds on that first introduced by Kim *et al.* (2004) and uses vertical velocity recorded by a seismometer to verify the frequency response of a nearby infrasound station. It uses the averaged cross-spectral density to reduce the response estimate variance and the coherence as a measure of confidence for each estimate. We only include time–frequency segments with high coherence in our response estimate. This method produces high-quality (<5%) estimates of broadband frequency response when sufficient SNR and realistic acoustic impedance estimates are present. At stations COLA and I53 in interior Alaska, we derive high-quality frequency response estimates for all three earthquakes between ~0.02 and 1 Hz. These results are similar to those derived using complementary field-based techniques (Gabrielson, 2011) that rely on a separate reference sensor and ambient noise. When a reference sensor is not available, our method can provide an independent assessment of the infrasound metadata and station performance. This is particularly useful for large networks, such as that in Alaska, and in places where data quality or metadata are unknown. Similarly, we use a single seismometer at COLA to derive robust frequency response estimates at all eight I53 infrasound elements spread over an ~2 × 2 km area, suggesting this method is viable for cross-array calibration. We believe this method could be applied to other IMS infrasound arrays to help determine the frequency response and meet calibration requirements, as well as assist with data quality assessments.

When applied to all colocated seismoacoustic stations in Alaska, our method produced high-quality frequency response estimates at numerous stations. As expected, higher coherence is present at lower frequencies and at quieter stations. We identified multiple problems with both station metadata and installation. Comparing our results to noise levels in PPSDs was helpful in identifying the issues. Using our results, we worked with local network operators to help correct invalid metadata and identify station installation issues.

Although our method is promising for infrasound station characterization, there are a number of challenges and areas of future work. First, the method relies on relatively large earthquakes and long (minutes) duration signals. High-magnitude earthquakes will generate broadband, high-amplitude seismic and acoustic signals, whereas lower magnitude events will not. Regions of high seismicity, such as Alaska, seem well suited to our method. In this study, surface waves provided the majority of the coherent signals used for response estimation, which limits higher frequency estimates. Even with large earthquakes and considerable ground motion, SNR can be problematic. Infrasound data are often dominated by noise from wind and other sources, and our method and data set were not sufficient for adequate frequency response estimation for many noisy stations (Fig. 6). Achieving high-accuracy (i.e., <5%) frequency response estimates is possible but also challenging. In addition to sufficient SNR, accurate estimates of local temperature and pressure are needed for accurate infrasound frequency response estimates. Higher frequency response estimates are also elusive due to the limited high-frequency seismic energy recorded at the distances we examined. Long-term stability and calibration accuracy of the seismometer also needs to be considered. Improved, careful signal processing techniques may resolve some of these issues, but we note true “calibration” below 5% will likely involve future work and careful processing.

Seismoacoustic coupling is being increasingly used to study subsurface processes on Earth and for potential future

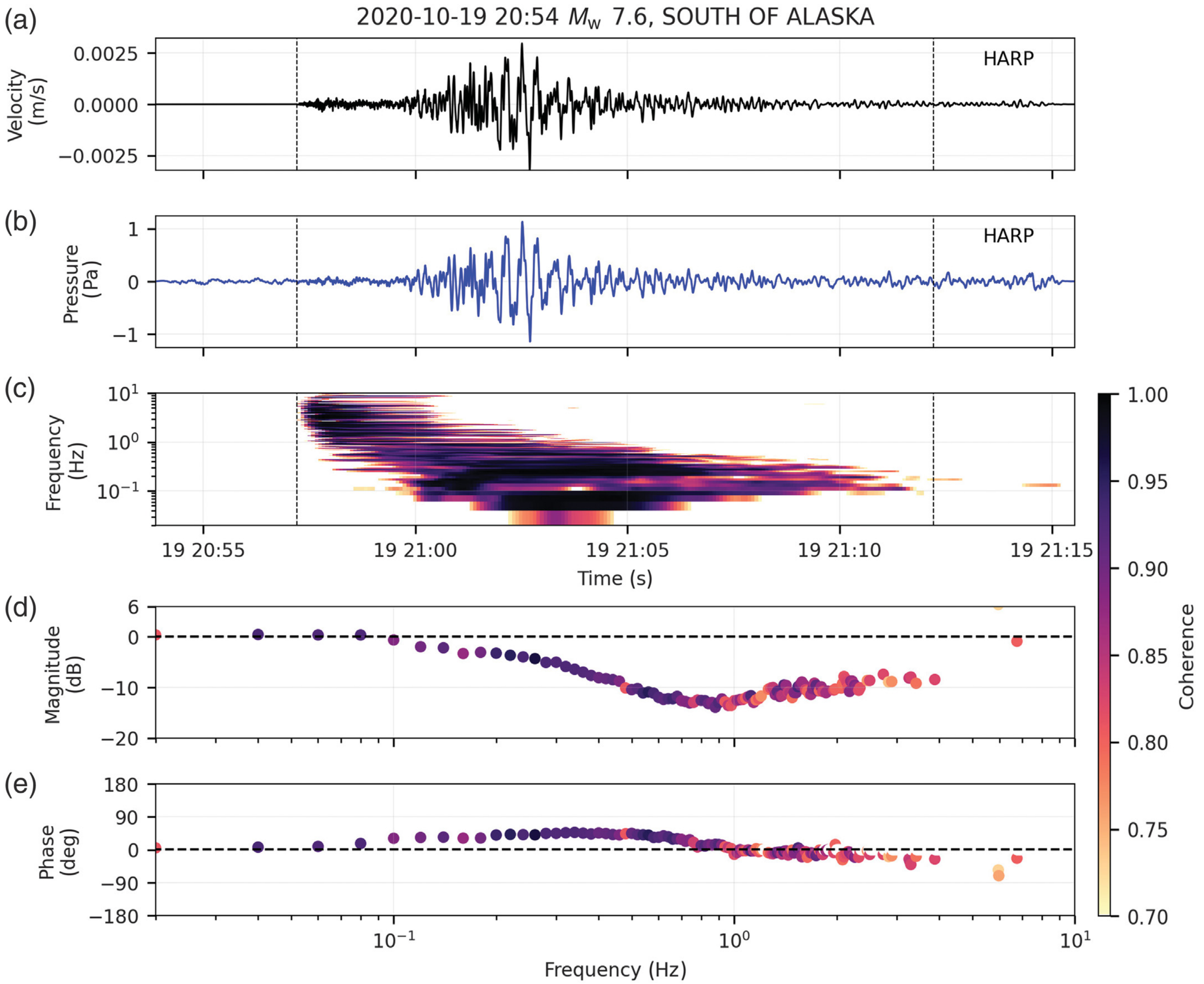

Figure 9. Waveforms, coherence, and frequency response for the 19 October 2020 M_w 7.8 earthquake at HARP. (a,b) Seismic and infrasound data, (c) coherence, (d) magnitude, and (e) phase. The response shows a notable deviation in magnitude and phase that varies with frequency.

experiments on other planets (e.g., Brissaud *et al.*, 2021). Our study shows how seismoacoustic coupling can be used to help characterize infrasound frequency response and data quality, but our processing technique could also be utilized for careful examination of seismoacoustic coupling. We encourage more colocated seismoacoustic deployments to facilitate study of seismoacoustic and acoustic-seismic coupling more generally. Emerging techniques in these fields such as McKee *et al.* (2018) and K. A. Macpherson *et al.* (unpublished manuscript, see Data and Resources) are complementary to traditional infrasound array and seismic network techniques. Further study on the physics of seismoacoustic coupling should also occur to better understand the limits and potential of this phenomena.

DATA AND RESOURCES

Seismic and infrasound data analyzed here are part of the Alaska Earthquake Center (AEC, doi: 10.7914/SN/AK), Alaska Volcano Observatory (AVO, doi: 10.7914/SN/AV), the Global Seismographic Network–Incorporated Research Institutions for Seismology (IRIS)/International Deployment of Accelerometers (IDA) (doi: 10.7914/SN/II) and IRIS/U.S. Geological Survey (USGS) (doi: 10.7914/SN/IU), and the International Monitoring Systems (IMSs, no DOI registered) networks, and these data are available from the IRIS Data Management Center (DMC) (http://ds.iris.edu/ds/nodes/dmc/, last accessed January 2023). The unpublished manuscript by K. A. Macpherson, D. Fee, J. R. Coffey, and A. J. Witsil, “Using ground-motion generated local infrasound to estimate seismic velocity and earthquake magnitudes,” submitted to *Bull. Seismol. Soc. Am.*

DECLARATION OF COMPETING INTERESTS

The authors acknowledge that there are no conflicts of interest recorded.

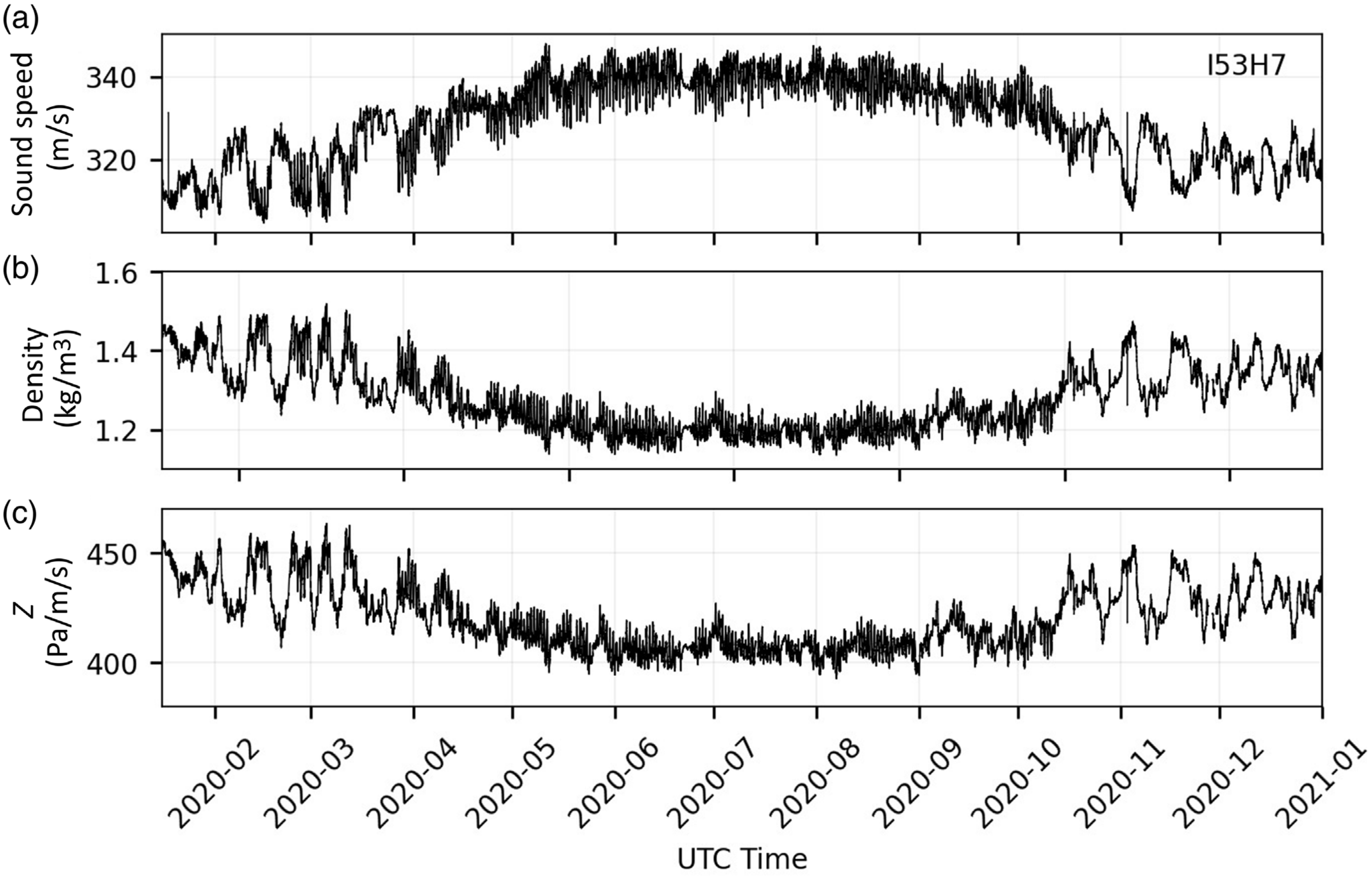

Figure 10. (a) Sound speed, (b) air density, and (c) impedance contrast for I53H7 for 2020.

ACKNOWLEDGMENTS

Two anonymous reviewers provided valuable comments that improved the article. This work was supported by the Nuclear Arms Control Technology (NACT) Program at Defense Threat Reduction Agency (DTRA) under Contract Numbers HDTRA121C0030 and HQ003421F0112. Approved for public release; distribution is unlimited. The majority of the AK infrasound stations were supported under the National Science Foundation (NSF) Award Number 2024208. We used ObsPy (Beyreuther *et al.*, 2010) extensively for data analysis and PyGMT (Uieda *et al.*, 2021) to create Figures 1 and 6. Members of the Wilson Alaska Technical Center provided valuable feedback during the analysis stage of this work. We also thank members of the Alaska Earthquake Center (AEC) in diagnosing and correcting station and metadata issues. The majority of the analysis was done at the University of Alaska Fairbanks, located on the ancestral land of the Dena people of the lower Tanana River.

REFERENCES

Arrowsmith, S. J., J. B. Johnson, D. P. Drob, and M. A. H. Hedlin (2010). The seismoacoustic wavefield: A new paradigm in studying geophysical phenomena, *Rev. Geophys.* **48,** doi: 10.1029/2010rg000335.

Assink, J. D., G. Averbuch, P. S. Smets, and L. G. Evers (2016). On the infrasound detected from the 2013 and 2016 DPRK's underground nuclear tests, *Geophys. Res. Lett.* **43,** no. 7, 3526–3533, doi: 10.1002/2016GL068497.

Averbuch, G., R. M. Waxler, P. S. M. Smets, and L. G. Evers (2020). Probabilistic inversion for submerged source depth and strength from infrasound observations, *J. Acoust. Soc. Am.* **147,** no. 2, 1066–1077, doi: 10.1121/10.0000695.

Beyreuther, M., R. Barsch, L. Krischer, T. Megies, Y. Behr, and J. Wassermann (2010). ObsPy: A Python toolbox for seismology, *Seismol. Res. Lett.* **81,** no. 3, 530–533.

Bishop, J. W., D. Fee, R. Modrak, C. Tape, and K. Kim (2022). Spectral element modeling of acoustic to seismic coupling over topography, *J. Geophys. Res.* **127,** no. 1, doi: 10.1029/2021JB023142.

Brissaud, Q., S. Krishnamoorthy, J. M. Jackson, D. C. Bowman, A. Komjathy, J. A. Cutts, Z. Zhan, M. T. Pauken, J. S. Izraelevitz, and G. J. Walsh (2021). The first detection of an earthquake from a balloon using its acoustic signature, *Geophys. Res. Lett.* **48,** no. 12, e2021GL093013, doi: 10.1029/2021GL093013.

Brown, D., L. Ceranna, M. Prior, P. Mialle, and R. J. Le Bras (2014). The IDC seismic, hydroacoustic and infrasound global low and high noise models, *Pure Appl. Geophys.* **171,** nos. 3/5, 361–375.

Busby, R. W., and K. Aderhold (2020). The Alaska transportable array: As built, *Seismol. Res. Lett.* doi: 10.1785/0220200154.

Donn, W. L., and E. S. Posmentier (1964). Ground-coupled air waves from the Great Alaskan earthquake, *J. Geophys. Res.* **69,** no. 24, 5357–5361, doi: 10.1029/jz069i024p05357.

Elliott, J. L., R. Grapenthin, R. M. Parameswaran, Z. Xiao, J. T. Freymueller, and L. Fusso (2022). Cascading rupture of a megathrust, *Sci. Adv.* **8,** no. 18, eabm4131, doi: 10.1126/sciadv.abm4131.

Fee, D., R. Waxler, J. Assink, Y. Gitterman, J. Given, J. Coyne, P. Mialle, M. Garces, D. Drob, D. Kleinert, *et al.* (2013). Overview of the 2009 and 2011 Sayarim infrasound calibration experiments, *J. Geophys. Res.* **118,** no. 12, doi: 10.1002/jgrd.50398.

Gabrielson, T. B. (2011). In situ calibration of atmospheric-infrasound sensors including the effects of wind-noise-reduction pipe systems, *J. Acoust. Soc. Am.* **130,** no. 3, 1154–1163.

Green, D. N., J. Guilbert, A. Le Pichon, O. Sebe, and D. Bowers (2009). Modelling ground-to-air coupling for the shallow M-L 4.3 Folkestone, United Kingdom, earthquake of 28 April 2007, *Bull. Seismol. Soc. Am* **99,** no. 4, 2541–2551.

Green, D. N., A. Nippress, D. Bowers, and N. D. Selby (2021). Identifying suitable time periods for infrasound measurement system response estimation using across-array coherence, *Geophys. J. Int.* **226,** no. 2, 1159–1173, doi: 10.1093/gji/ggab155.

Ichihara, M., M. Takeo, A. Yokoo, J. Oikawa, and T. Ohminato (2012). Monitoring volcanic activity using correlation patterns between infrasound and ground motion, *Geophys. Res. Lett.* **39,** L04304, doi: 10.1029/2011GL050542.

Kennett, B. L. N., and E. R. Engdahl (1991). Traveltimes for global earthquake location and phase identification, *Geophys. J. Int.* **105,** no. 2, 429–465.

Kim, T. S., C. Hayward, and B. Stump (2004). Local infrasound signals from the Tokachi-Oki earthquake, *Geophys. Res. Lett.* **31,** no. 20, 10–13, doi: 10.1029/2004GL021178.

Le Pichon, A., P. Herry, P. Mialle, J. Vergoz, N. Brachet, M. Garcés, D. Drob, and L. Ceranna (2005). Infrasound associated with 2004-2005 large Sumatra earthquakes and tsunami, *Geophys. Res. Lett.* **32,** no. 19, 1–5, doi: 10.1029/2005GL023893.

Macpherson, K. A., J. R. Coffey, A. J. Witsil, D. Fee, S. Holtkamp, S. Dalton, H. McFarlin, and M. West (2022). Ambient infrasound noise, station performance, and their relation to land cover across Alaska, *Seismol. Res. Lett.* **93,** no. 4, 2239–2258, doi: 10.1785/0220210365.

Marty, J. (2018). The IMS infrasound network: Current status and technological developments, in *Infrasound Monitoring for Atmospheric Studies: Challenges in Middle Atmosphere Dynamics and Societal Benefits*, A. Le Pichon, E. Blanc, and A. Hauchecorne (Editors), Second Ed., Springer, Cham, Switzerland, doi: 10.1007/978-3-319-75140-5_1.

Marty, J., S. Denis, T. Gabrielson, M. Garcés, and D. Brown (2016). Comparison and validation of acoustic response models for wind noise reduction pipe arrays, *J. Atmos. Ocean. Technol.* **34,** no. 2, 401–414, doi: 10.1175/jtech-d-16-0118.1.

McKee, K., D. Fee, M. Haney, R. S. Matoza, and J. Lyons (2018). Infrasound signal detection and back azimuth estimation using ground-coupled airwaves on a seismo-acoustic sensor pair, *J. Geophys. Res.* **123,** no. 8, 6826–6844, doi: 10.1029/2017JB015132.

McNamara, D. E., and R. P. Buland (2004). Ambient noise levels in the continental United States, *Bull. Seismol. Soc. Am.* **94,** no. 4, 1517–1527.

Merchant, B. J., and K. D. McDowell (2014). MB3a infrasound sensor evaluation, *Technical Rept. Sandia National Lab. (SNL-NM)*, Albuquerque, New Mexico.

Merchant, B. J., R. K. Rembold, and G. W. Slad (2017). Infrasound isolation chamber for improved sensor calibration, *Technical Rept. Sandia National Lab. (SNL-NM)*, Albuquerque, New Mexico.

Nief, G., C. Talmadge, J. Rothman, and T. Gabrielson (2018). New generations of infrasound sensors: Technological developments and calibration, in *Infrasound Monitoring for Atmospheric Studies: Challenges in Middle Atmosphere Dynamics and Societal Benefits*, A. Le Pichon, E. Blanc, and A. Hauchecorne (Editors), Second Ed., Springer, Cham, Switzerland, doi: 10.1007/978-3-319-75140-5_2.

Pierce, A. D. (2019). *Acoustics: An Introduction to its Physical Principles and Applications*, Springer, Cham, Switzerland.

Power, J. A., M. M. Haney, S. M. Botnick, J. P. Dixon, D. Fee, A. M. Kaufman, D. M. Ketne, J. J. Lyons, T. Parker, J. F. Paskievitch, *et al.* (2020). Goals and development of the Alaska volcano observatory seismic network and application to forecasting and detecting volcanic eruptions, *Seismol. Res. Lett.* **91,** no. 2A, 647–659, doi: 10.1785/0220190216.

Shani-Kadmiel, S., J. D. Assink, P. S. Smets, and L. G. Evers (2018). Seismoacoustic coupled signals from earthquakes in Central Italy: Epicentral and secondary sources of infrasound, *Geophys. Res. Lett.* **45,** no. 1, 427–435, doi: 10.1002/2017GL076125.

Uieda, L., D. Tian, W. J. Leong, L. Toney, W. Schlitzer, M. Grund, D. Newton, M. Ziebarth, M. Jones, and P. Wessel (2021). PyGMT: A Python interface for the generic mapping tools, *Zenodo* doi: 10.5281/zenodo.7481934.

U.S. Geological Survey (USGS) (2017). Advanced National Seismic System (ANSS) comprehensive catalog of earthquake events and products, various, doi: 10.5066/F7MS3QZH.

Watada, S., T. Kunugi, K. Hirata, H. Sugioka, K. Nishida, S. Sekiguchi, J. Oikawa, Y. Tsuji, and H. Kanamori (2006). Atmospheric pressure change associated with the 2003 Tokachi-Oki earthquake, *Geophys. Res. Lett.* **33,** no. 24, doi: 10.1029/2006GL027967.

Xiao, Z., J. T. Freymueller, R. Grapenthin, J. L. Elliott, C. Drooff, and L. Fusso (2021). The deep Shumagin gap filled: Kinematic rupture model and slip budget analysis of the 2020 Mw 7.8 Simeonof earthquake constrained by GNSS, global seismic waveforms, and floating InSAR, *Earth Planet. Sci. Lett.* **576,** 117241, doi: 10.1016/j.epsl.2021.117241.

Manuscript received 4 November 2022